

A Wavefield Correlation Approach to Improve Sound Speed Estimation in Ultrasound Autofocusing

Louise Zhuang, Samuel Beuret, Ben Frey, Saachi Munot, and Jeremy J. Dahl

Abstract—Aberration often degrades ultrasound image quality when beamforming does not account for wavefront distortions. In the past decade, local sound speed estimators have been developed for distributed aberration correction throughout a medium. Recently, iterative sound speed optimization approaches have achieved more accurate estimates than earlier approaches, but these newer methods still struggle with decreased accuracy for media with reverberation clutter and large sound speed changes. To address these challenges, we propose using a wavefield correlation (WFC) beamforming approach when performing sound speed optimization. WFC correlates simulated forward-propagated transmit wavefields and backwards-propagated receive wavefields in order to form images. This process more accurately models wave propagation in heterogeneous media and can decrease diffuse clutter due to its spatiotemporal matched filtering effect. This beamformer is implemented using auto-differentiation software to then perform gradient descent optimization, using a total-variation regularized common midpoint phase focus metric loss, on the local sound speed map used during beamforming. This approach is compared to using delay and sum (DAS) with straight-ray time delay calculations in the same sound speed optimization approach on a variety of simulated, phantom, and *in vivo* data with large sound speed changes and clutter. Results show that using WFC decreases sound speed estimation error, and using the estimates for aberration correction improves image resolution and contrast. These promising results have potential to improve pulse-echo imaging for challenging clinical scenarios.

Index Terms—aberration correction, angular spectrum, clutter, Fourier split step, gradient descent, image focus optimization, sound speed estimation, wavefield correlation

I. INTRODUCTION

Aberration occurs when an ultrasound beam is not properly focused during beamforming, typically due to heterogeneous sound speed in the media that does not align with the beamforming sound speed. During the image reconstruction process, this impaired focus can cause degradation in the image quality, including decreased resolution, visibility, and contrast [1]. Clinically, aberration can impact medical diagnosis, especially in cases of high depth *in vivo* imaging, such as

This work was supported in part by the National Science Foundation Graduate Research Fellowship under Grant No. DGE-1656518 and National Institutes of Health Grant R01-027100.

Louise Zhuang is with the Department of Electrical Engineering, Stanford University, Stanford, CA 94305.

Samuel Beuret and Jeremy J. Dahl are with the Department of Radiology, School of Medicine, Stanford University, Stanford, CA 94305.

Ben Frey is with the Department of Applied Physics, Stanford University, Stanford, CA 94305.

Saachi Munot is with the Department of Biomedical Engineering, Columbia University, New York, NY 10027

abdominal applications [2], [3], and in overweight or obese individuals. To alleviate these problems, aberration correction methods that compensate for the errors due to sound speed heterogeneity have been of high interest for many decades.

Recent approaches to performing distributed aberration correction involve the so-called "sound-speed-aware" beamformer, where a local sound speed estimate of the imaged medium is obtained, followed by beamforming with time delays calculated using the sound speed estimate to better focus the image throughout the medium [4]. Early pulse-echo local sound speed estimators that could be used for typical medical ultrasound applications were based on solving tomographic inversion problems [5]–[8] or estimating the depthwise global (cumulative) sound speed and performing Dix inversion to compute the local sound speed per depth [9], [10]. Although these early methods produced novel estimation results for the traditionally challenging pulse-echo imaging configuration, the estimates often had limited resolution and accuracy, especially when performing *in vivo* imaging. Nevertheless, from these estimates of the local sound speed, image reconstruction can be used to improve the image focus, often through delay-and-sum (DAS) beamforming but with assumed straight-ray or bent-ray (refracted) propagation paths to compute time delays [11], [12]. Although these methods could be memory- or time-consuming when computing propagation paths at high resolutions, even with not completely accurate local sound speed maps [13], [14], the image quality could have a visible improvement.

To improve upon sound speed inversion methods, iterative closed-loop versions of sound speed estimators have been proposed. An iterative version of pulse-echo tomographic sound speed estimation (iterative CUTE) was developed in [15]. The final predictions from this approach have increased accuracy compared to the prior CUTE model [7] because repeatedly updating the phase shifts for the inversion process using the previously estimated sound speed map alleviates the estimation bias from the initial assumed sound speed. Similarly, [14] improves upon [13], in part by iteratively calculating aberration delays from beamformed data and updating the sound speed estimate in a closed loop. While many of these estimators utilize the relationship between phase shifts, or delays, caused by aberration and the local sound speed in the medium to solve an inversion problem, some of the latest aberration correction approaches optimize an image focus criterion with respect to the local sound speed instead. In earlier decades, optimizing a focus criterion was used for simpler phase-screen

models of aberration [16], [17], but has recently been expanded to more distributed correction methods [18]. However, these approaches did not incorporate local sound speed to the image reconstruction process. Recently, we introduced ultrasound autofocusing, a distributed aberration correction technique that ties image focusing criteria to gradient-descent-based sound speed estimation to iteratively update a local sound speed estimate and apply DAS beamforming via delays calculated by a straight-ray model of wave propagation [19]. This method has been shown to produce excellent distributed aberration correction. However, while the sound speed estimation it produces is improved significantly over prior models, the estimation is not entirely accurate because the method does not explicitly optimize for the correct local sound speed, but rather a local sound speed that is optimal for the focusing criterion. Additionally, this method can have difficulty accurately estimating sound speeds for regions with large sound speed differences from the mean global sound speed.

Estimation accuracy can also degrade with data corrupted by acoustic noise. As shown in [9], diffuse reverberation can significantly increase the bias in sound speed estimation due to signal multi-pathing and increased clutter that decreases signal coherence. Additionally, many sound speed estimators utilize a straight- or bent-ray DAS beamforming model to calculate time delays, which may not completely model actual wave propagation through complex heterogeneous media or media with large sound speed changes. However, an alternative beamforming strategy, referred hereafter as wavefield correlation (WFC), can be used to model more complex wave propagation, such as diffraction. Wavefield correlation, also known as shot-profile and reverse-time migration in geophysics [20], consists of simulating the forward propagation of the transmit wavefields and backpropagation of the receive wavefields, followed by the correlation of those wavefields at each propagation step to form the final image axially [13], [21], [22]. This approach can more accurately represent wave propagation during the image reconstruction process and correct for aberration given an estimated local sound speed map [13]. Due to the properties of the angular spectrum, this method can also reduce the effect of diffuse reverberation in the final beamformed data [23] by acting as a spatial matched filter.

In this manuscript, we extend our prior work in [23] to incorporate an image-quality optimization sound speed estimation approach that uses wavefield correlation as the beamformer and the differentiable beamformer approach to improve local sound speed estimates in cluttered and complex media. While this approach is similar to [24] in its usage of WFC as a beamformer and iteratively updating the sound speed model, our work differs fundamentally in the optimization criterion and how the sound speed is updated. We cover the background theory and implementation in Section II and describe simulation, phantom, and *in vivo* data experiments in Section III that demonstrate improved estimation accuracy and image quality improvements in Section IV.

II. THEORY

In this section, we explain the wavefield correlation beamforming approach, and then describe how it is integrated into

a sound speed optimization method to perform aberration correction and local sound speed estimation. The final process used for estimating the local sound speed is illustrated in Figure 1.

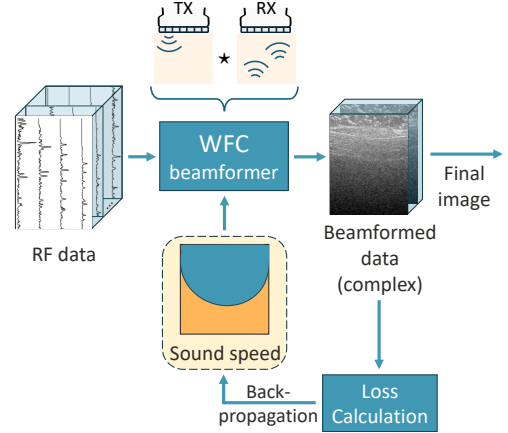


Fig. 1: Diagram of the sound speed optimization approach used in this work. The common midpoint phase error is used as the image focus criterion minimized in the optimization objective function. The beamforming process to obtain the focus criterion, using WFC, is tracked using auto-differentiation software, which is then used to backpropagate the loss gradient to update the local sound speed estimation. This iterative gradient-descent-based optimization process then repeats until the estimations have reasonably converged to a local minimum.

A. Wavefield Correlation Beamformer

Image reconstruction by correlating transmit and receive wavefields has previously been presented for ultrasound applications in [21], [22], [25]. The implementation used in this work follows [13], where transmit pulses are forward propagated and the received data are backward propagated through heterogeneous media using a Fourier domain simulator, and the two wavefields are correlated and summed to form each depth-wise row in the image. We briefly review this approach below, but the reader is referred to Schwab et al. [21] and Ali et al. [13], [22] for a more detailed discussion.

1) *Wavefield Simulations*: To obtain the transmit and receive wavefields, $p_{tx}(x, z, t)$ and $p_{rx}(x, z, t)$, respectively, for azimuth dimension x , depth dimension z , and time dimension t , the known transmit pulse sequence $p_{tx}(x, z = 0, t)$ or channel data $p_{rx}(x, z = 0, t)$ at the surface of the transducer is propagated via simulation. Transmit pulses are forward propagated through the heterogeneous media, while the received radiofrequency (RF) data is backward propagated through the same medium. The particular simulator used for this work is a Fourier-domain split-step angular spectrum method (ASM), which is less computationally demanding than a full finite-difference-time-domain (FDTD) simulator but can still model wave propagation through a heterogeneous medium, albeit without multiple reflections [26]. For simplicity, the type of angular spectrum method used in this work does not incorporate attenuation or non-linearity.

To propagate a wavefield $p(x, z, t)$ using the split-step angular spectrum method for a linear transducer, the wavefield is first transformed into the angular spectrum domain through a 2D Fourier transform:

$$p(k_x, z, f) = \mathcal{F}_{x \rightarrow k_x} \{ \mathcal{F}_{t \rightarrow f} [p(x, z, t)] \}. \quad (1)$$

The wave is then propagated to the next depth sample by accounting for diffraction through a medium with a constant sound speed:

$$p_{diff.r.}(k_x, z + \Delta z, f) = \exp(\mp j 2\pi \Delta z \sqrt{f^2 \bar{u}^2(z) - k_x^2}) * p(k_x, z, f), \quad (2)$$

where the $-$ sign is used for forward propagation, and the $+$ sign is used for backward propagation. Here, the slowness, $u(x, z) = 1/c(x, z)$, for a medium with local sound speed $c(x, z)$ is decomposed as $u(x, z) = \bar{u}(z) + \Delta u(x, z)$ into a mean slowness and a differential slowness, respectively. The mean slowness is used for this initial propagation step.

Refraction during the propagation process from an inhomogeneous medium is then applied by taking the inverse Fourier transform in the azimuth dimension

$$p_{diff.r.}(x, z + \Delta z, f) = \mathcal{F}_{k_x \rightarrow x}^{-1} [p_{diff.r.}(k_x, z + \Delta z, f)] \quad (3)$$

and multiplying the result by a phase term with the differential slowness

$$p(x, z + \Delta z, f) = \exp(\mp j 2\pi f \Delta z \Delta u(x, z)) * p_{diff.r.}(x, z + \Delta z, f). \quad (4)$$

These propagation steps are iterated through successive depths to obtain wavefields for the entire region of interest.

2) *Image Reconstruction*: Wherever a scatterer is located in the medium, a wavefront peak will occur at that location in both the transmit and receive wavefields at the exact same time [27]. Thus, to reconstruct an image, $I(x, z)$, from these wavefields, the transmit and receive wavefields are correlated at each image location and summed over all frequencies

$$I(x, z) = \int_{-\infty}^{\infty} p_{tx}(x, z, f) p_{rx}^*(x, z, f) df. \quad (5)$$

This process is equivalent to summing the correlations over all time [22].

3) *Beamformer Advantages*: This beamforming approach has several advantages that can benefit sound speed estimation and resulting aberration correction. The beamforming process results in a spatio-temporal matched filtering effect from correlating the ideal transmit wavefield with the backpropagated receive data, which can potentially reduce diffuse reverberation noise in the resulting image [23]. Additionally, since a local sound speed map can be used for the simulations, the wave propagation with refractive and diffractive effects of heterogeneous media is more accurately modeled compared to other beamforming approaches, such as DAS using straight ray paths to calculate time delays. Finally, all steps taken during the beamforming process are differentiable, allowing integration into the autofocusing approach we have previously developed for simultaneous aberration correction and sound speed estimation [19].

B. Gradient-Descent-Based Sound Speed Estimation

Sound speed estimation for this work follows a gradient descent optimization approach proposed in [19]. This method optimizes an image focusing metric relative to the local sound speed map, and updates the sound speed map in the same way as neural network loss backpropagation to minimize the loss function. All operations to calculate the final loss metric involving the local sound speed are tracked in a software package with automatic differentiation functionality, and the computed gradient value from these operations is used to update the local sound speed map. The process then repeats iteratively, much like neural network training, using the updated sound speed map to compute the loss metric and then auto-differentiation to obtain the gradient for updating the sound speed map.

The optimized loss metric used for this work is the combination of the common midpoint phase and the total variation of the sound speed map:

$$\mathcal{L}(c) = \mathcal{L}_{CMPE}(c) + \gamma \mathcal{R}_{TV}(c), \quad (6)$$

where c represents the local sound speed map, \mathcal{L}_{CMPE} represents a common midpoint phase error image focus metric, γ represents a scalar regularization weight, and \mathcal{R}_{TV} represents anisotropic total variation regularization.

1) *Common Midpoint Phase Error*: The correlation of beamformed pressure signals between two receive locations, given as

$$R(\mathbf{x}_1, \mathbf{x}_2) = \langle P(\mathbf{x}_1, \mathbf{x}_2) P^*(\mathbf{x}_2) \rangle, \quad (7)$$

for pressure field P at spatial locations \mathbf{x}_1 and \mathbf{x}_2 , is formulated for pulse-echo ultrasound using the van Cittert-Zernike theorem through an aberrating layer in [28] as:

$$R(\mathbf{x}_1, \mathbf{x}_2) = A \cdot e^{j[\phi(\mathbf{x}_1) - \phi(\mathbf{x}_2)]} \cdot e^{j \frac{\pi}{\lambda z} (\mathbf{x}_1 \mathbf{x}_1 - \mathbf{x}_2 \mathbf{x}_2)} \cdot \int |P_i(\mathbf{u})|^2 e^{j 2\pi \frac{\mathbf{x}_1 - \mathbf{x}_2}{\lambda z} \mathbf{u}} d\mathbf{u}. \quad (8)$$

In this equation, A is the resulting amplitude term, ϕ is the aberration expressed as a phase, λ is the wavelength, z is the depth, and P_i is the transmitted pressure field. The integral term represents the Fourier transform of the source pressure field intensity, per the van Cittert-Zernike theorem. The second exponential term outside of the Fourier transform represents a location-dependent phase term based on the Fresnel approximation. The first exponential then represents any remaining phase difference between the two receive locations due to aberration. When the two receive locations share a common midpoint about the transducer axis, i.e.,

$$\mathbf{x}_1 = \mathbf{x}_m + \Delta x, \quad (9)$$

$$\mathbf{x}_2 = \mathbf{x}_m - \Delta x, \quad (10)$$

and the data is beamformed, all phase terms except the first term cancel out or become deterministic. The first phase term thus accounts for any beamforming inaccuracies that cause aberration in the final beamformed data. Under perfect focusing, the first phase term should reduce to 0. The mean phase difference between common midpoint signals, called the common midpoint phase error [19], is proposed as a measure

of the focusing quality of the beamformer and utilized as an optimization objective, i.e.,

$$\mathcal{L}_{CMPE} = \angle R(\mathbf{x}_1, \mathbf{x}_2). \quad (11)$$

In Simson et al. [19], the common midpoint phase error for the beamformed data over all common midpoint subapertures of size 17 elements was used after excluding values where the correlation coefficient at that location was lower than 0.9 to exclude noisy signals. Similarly, the work in this paper uses this filtered version of the common midpoint phase error (CMPE), which is minimized during the optimization process. This metric is computed through software beamforming of the data using WFC. Separate simulations are performed for each subaperture considered, and both the ASM simulations and correlation process for final image formation are composed of differentiable operations.

2) *Total Variation Regularization*: Since pulse-echo sound speed estimation is ill-posed, minimizing the CMPE by itself is not sufficient to obtain a reasonable local sound speed estimate. To regularize the objective function for the optimization problem, a weighted form of anisotropic total variation is used

$$\mathcal{R}_{TV} = \sum_{i=1}^M \sum_{j=1}^N \alpha_x |D_x(i, j)| + \alpha_z |D_z(i, j)|, \quad (12)$$

where

$$D_x(i, j) = c(x_i, z_j) - c(x_{i-1}, z_j), \quad (13)$$

is the first difference of the discrete sound speed map, c , in the lateral dimension x , containing M samples;

$$D_z(i, j) = c(x_i, z_j) - c(x_i, z_{j-1}), \quad (14)$$

is the first difference of the sound speed map in the axial dimension, z , containing N samples; α_x is the relative lateral difference weighting; and α_z is the relative axial difference weighting. By enforcing smoothness in the sound speed map using total variation regularization, the resulting sound speed map is relatively more homogeneous while still retaining boundary edges, which is more physically reasonable. Additionally, the image visually appears more reasonable without major distortions.

III. METHODS

A. Optimizer Configuration

The sound speed optimization pipeline, based on [19] but using WFC, was implemented using an Adam optimizer with default parameters and the loss function in Equation 6. A learning rate scheduler was used to ramp up and slightly decay the learning rate based on the iteration number. A linear warmup was used starting from a learning rate of 0.005 and ending at a maximum learning rate of 0.015. After 110 iterations, the learning rate would then exponentially decay by a rate of 0.01275. For simulation and phantom experiments, the weight γ for the total variation regularization was set to 0.3 as the minimal amount to consistently result in visually smooth sound speed estimation. For the thyroid *in vivo* acquisitions with increased reverberation noise, the weight was set to $\gamma = 0.75$ to more strongly enforce smoothness in the sound

speed estimates. For all data, the dimensional components of the total variation regularization in Equation 12 were weighted with $\alpha_x = 5$ and $\alpha_z = 1$ to follow a more layer-wise sound speed structure, as in [19]. The phase error was computed in 2D kernels placed on a grid with 1 mm spacing laterally and axially. Each individual kernel had a 2λ length and $2\lambda/3$ intra-kernel point spacing in both lateral and axial dimensions. The sound speed map was defined with a grid resolution of 1 mm². Both grids spanned the axial and lateral range shown by the beamformed images in the results section, which may differ from the field of view used in [19]. For display purposes only, the final sound speed estimates shown in this paper have been linearly interpolated to match the beamformed image grid. The initial constant sound speed used for beamforming and a constant time offset applied to alleviate global sound speed bias were simultaneously swept to optimize the CMPE metric. The sound speeds were swept from 1350 to 1750 m/s with a step size of 2 m/s, and the time offsets were swept from -4.9 to 0.3 μ s with a step size of 0.1 μ s. A finer phase error loss grid with 2λ kernel spacing so that the kernels border each other was used for the initial sweep due to the lack of memory constraints for the initialization. The optimization loop was run for 200 iterations for simulation data and 100 iterations for scanner data. These cutoffs were determined by the number of iterations for the sound speed maps to generally settle at a local optimum.

For the split step angular spectrum propagation used during WFC beamforming, the simulation grid has a spacing of one-half the element pitch laterally and $\lambda/2$ axially, with a Butterworth anti-aliasing filter as in [22] applied laterally during the propagation process to prevent wraparound artifacts. For consistency and memory constraints, the center 128 elements were used for beamforming all data, except for the rat acquisitions described in the following subsection, which were beamformed using 160 elements to encompass a larger lateral span due to the shallow imaging depth.

B. Experiments

The optimization pipeline above was compared to using DAS with time delays calculated using a straight-ray travel path assumption through the medium as in [19], with otherwise the same initialization values and optimizer setup as described above. An f/# of 1 was used to calculate the common midpoint phase error criterion when using DAS, and 48 points per ray were used for calculating the time delays. Performance between using the two beamformers for optimization was compared for simulation, phantom, and *in vivo* data with reverberation clutter and sound speed heterogeneities.

1) *Simulation*: Fullwave 2 [29], [30] 2D FDTD simulations of a full synthetic aperture transmit sequence using a linear array were run with the transducer and transmit parameters included in Table I. Two simulations used segmented abdominal wall media with acoustical properties described in [31], shrunken axially to reduce the total wall thickness to 10 mm. The media below the wall then comprised of (a) a circular sound speed inclusion with a 5 mm diameter and 1570 m/s sound speed against a background of 1540 m/s, and (b) a two

layer medium with sound speeds of 1420 m/s and 1555 m/s. The density was set to 1000 kg/m³ for the background region in (a) and the first layer in (b). The densities of the second layer and inclusion were calculated so the impedance would match the background and first layer, respectively. The abdominal wall tissue was assigned acoustical parameters based on [31]. All other regions were simulated with a constant 0.10 dB/MHz/cm attenuation and 0 nonlinearity. A Gaussian blur with radius 7.5 pixels was additionally applied to the acoustic parameter maps to reduce visible reflections below the abdominal wall. The simulations used 18 scatterers per resolution cell and had a grid spacing of 0.013 mm².

TABLE I: Simulated Transducer and Transmit Parameters

Parameter	Value
Transmit Center Frequency	5.0 MHz
No. Cycles	2
Fractional Bandwidth	93.33%
No. Elements	192
Element Pitch	0.2 mm
Sampling Frequency	32.08 MHz

2) *Phantom*: To evaluate performance on phantom data, full synthetic aperture linear array acquisitions of two types of phantoms using a Verasonics Vantage 256 scanner (Kirkland, WA) were evaluated. A chicken layer between 10-15 mm thick was placed above an ATS 549 phantom (Norfolk, VA), reused from [10] where RF channel data was collected using a full synthetic aperture sequence from a 192 element L12-3v array with a 5.95 MHz transmit center frequency and 25 MHz sampling frequency. The ground truth sound speed in the chicken layer was measured using a piston transducer driven by a pulser-receiver, with time delays measured with an oscilloscope as described in [32]. This setup contained reverberation from the chicken-phantom boundary, as well as a sizeable sound speed difference between the chicken at 1568.5 m/s and the phantom at 1450 m/s. The acquired data were demodulated and decimated by 2 prior to beamforming due to memory constraints. For WFC, the data were then remodulated prior to the simulation process.

Secondly, data from a fabricated gelatin phantom originally acquired in [24] were used to further analyze beamformer performance for heterogeneous media. Wire targets in the phantom serve as point targets, and inclusions made of a gelatin-alcohol mixture created sound speed heterogeneities. An L12-5v, 50 mm array was used to acquire the data with a 6.0 MHz transmit center frequency and 25 MHz sampling frequency.

3) *In Vivo*: Thyroid and carotid artery *in vivo* data from three patients was originally captured in [33] using a 128-element full synthetic aperture sequence on an L12-3v transducer with a Verasonics Vantage 256 system. A transmit center frequency of 5.95 MHz was used, with a sampling frequency of 25 MHz. Due to memory constraints, this data was demodulated and decimated by 2 prior to beamforming. These acquisitions contain reverberation clutter from superficial tissue that is visible in the vessel and anechoic nodules.

Additional rat liver data from [32] was used to analyze sound speed estimation performance for tissues with larger

sound speed changes. Data originally were captured with a full synthetic aperture sequence using 192 elements on an L12-3v transducer with a Verasonics Vantage 256 system. The center transmit frequency was 7.81 MHz, with a 31.25 MHz sampling frequency. The global liver sound speeds were determined *ex vivo* in a 37°C water tank using the same procedure as the meat-layer phantom data. Four liver lobes with sound speed differences up to approximately 30 m/s were observed.

4) *Evaluation Criteria*: The sound speed estimates and resulting beamformed images were compared between the two beamformers. For simulation and phantom data with a known ground truth sound speed, the mean (bias) and standard deviation of the error is evaluated, as well as the mean absolute error (MAE). For data containing point targets or similar small, strong reflectors, the full width at half maximum (FWHM) was used to evaluate resolution. Additionally, for the *in vivo* data with anechoic regions, the generalized contrast to noise ratio (gCNR) [34] was evaluated to analyze the improvement in contrast and visibility.

IV. RESULTS

A. Simulation

The local sound speed estimates for the inclusion (a) and layered media (b) under an abdominal wall are shown in Figure 2, with errors for the regions underneath the abdominal wall quantified in Table II. Most noticeably, the different sound speed regions are visually more distinguished with WFC compared to the straight-ray model with DAS. The reduction in bias with WFC is especially large for the circular sound speed inclusion in simulation (a) and the first, low sound speed layer in simulation (b). Although the bottom sound speed layer in (b) has a 10 m/s higher bias for the WFC estimation, the sound speed variation is lower compared to DAS, which has a higher error standard deviation. High sound speed corners, somewhat reminiscent of shallow-depth artifacts sometimes seen in tomographic sound speed estimators [7], are visible at the top of the WFC estimates for both simulations. This corner artifact appears to focus energy inwards, away from the lateral edges of the WFC beamformed image.

TABLE II: Simulation Region Sound Speed Estimation Error

Sim. Region	Beamformer	Bias	Std. Dev.	MAE
(a) Inclusion	DAS	-22.86	1.98	22.86
	WFC	-1.48	6.77	3.83
(a) Background	DAS	-12.52	3.65	12.57
	WFC	-8.78	6.47	9.19
(b) Top Layer	DAS	32.22	4.66	32.22
	WFC	-3.74	6.92	5.92
(b) Bottom Layer	DAS	-52.64	14.06	52.64
	WFC	-62.04	6.23	62.04

B. Phantom

The sound speed estimates for the chicken overlying the ATS 549 phantom are shown in Figure 3, with errors listed in Table III. The measured sound speeds for the meat and phantom regions are visualized on the leftmost plot in Figure 3, with the depth around the boundary excluded (shown in white)

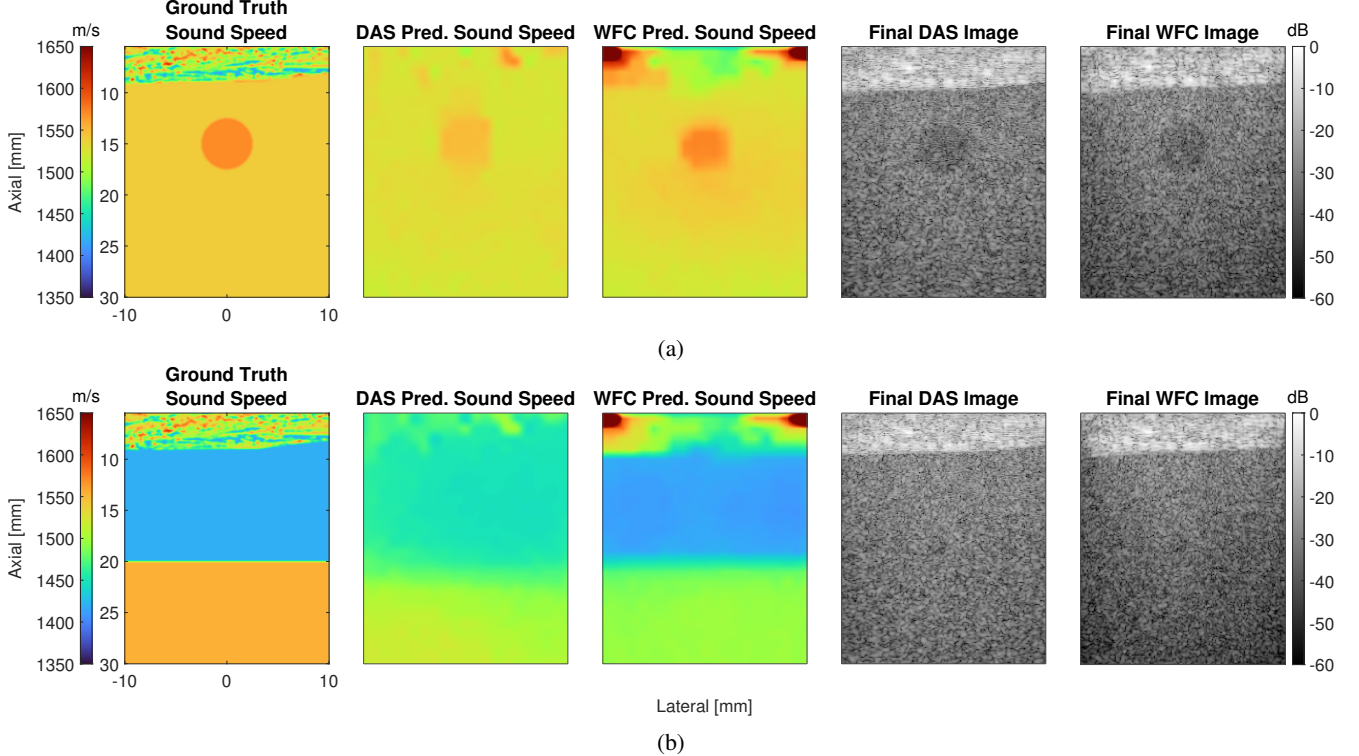


Fig. 2: Sound speed and final aberration-corrected image comparisons for abdominal wall simulations with a sound speed inclusion (a) and two sound speed layers (b), with the ground truth simulated sound speed shown on the leftmost panels. The sound speed estimates using WFC show clearer differentiation of different sound speed regions, with the abdominal wall, layers, and circular inclusion more accurately represented in the estimates compared to the DAS predictions.

due to the exact boundary location being unknown. Similarly to the abdominal wall simulations, the different sound speed regions are more visibly distinguishable in the WFC estimate compared to DAS, where the chicken region is more difficult to discern from the phantom region. Quantitatively, the bias is much higher in the chicken region for DAS than WFC. The standard deviation in the WFC sound speed estimation error, however, is higher than DAS due to the estimated sound speed decreasing in value towards the meat-phantom boundary. In the phantom region, which contains reverberation clutter from the chicken layer and phantom boundary, the DAS estimate has more than 10 m/s of bias, similar to previous sound speed estimation literature [9]. Conversely, the WFC estimate has lower bias in this region, although the standard deviation is slightly higher due to the sound speed dips visible around 15 to 20 mm in depth.

TABLE III: Phantom Sound Speed Estimation Error

Medium	Beamformer	Bias	Std. Dev.	MAE
Chicken	DAS	-92.74	4.84	92.74
	WFC	8.90	42.10	33.74
ATS 549	DAS	14.24	6.00	14.25
	WFC	0.76	11.78	7.25

The estimates for the fabricated alcohol-gelatin phantom are shown in Figure 4. Greater differentiation between the background and inclusion sound speeds are apparent in the WFC sound speed estimation, which has approximately a 25 m/s higher difference in sound speed than the DAS estimate.

The inclusion in the sound speed map also appears more circular in the WFC estimate compared to the DAS estimate. The elliptic eccentricity (ratio of the major axis to the minor axis) of the inclusion region was determined based on the region retained after thresholding the sound speed at 6 standard deviations above the estimated background sound speed. The central lesion eccentricity is 0.68 for DAS and 0.27 for WFC. Since a higher eccentricity represents a more oblong elliptical shape, the WFC inclusion is more circular in shape and more closely matches the expected inclusion shape. We have previously also observed the oblong shape of inclusions with the straight-ray model in our prior implementations [19]. Although the ground truth sound speeds for the regions were not measured, the effect of the difference in sound speed estimation can be observed in the final beamformed images of DAS and WFC, indicating, most likely, improved accuracy in the WFC estimation. Compared to using an initial homogeneous sound speed, the point targets when using a local sound speed estimate when beamforming have visible resolution improvements. However, the point targets on average have 0.24 mm lower lateral FWHM when using the WFC estimate compared to using the DAS estimate. Additionally, the point target brightness is relatively more bright compared to the background using the WFC sound speed estimate compared to the DAS estimate. The background speckle brightness, excluding the point targets, is approximately -40.9 dB for the initial constant sound speed beamformed image, -45.2 dB for

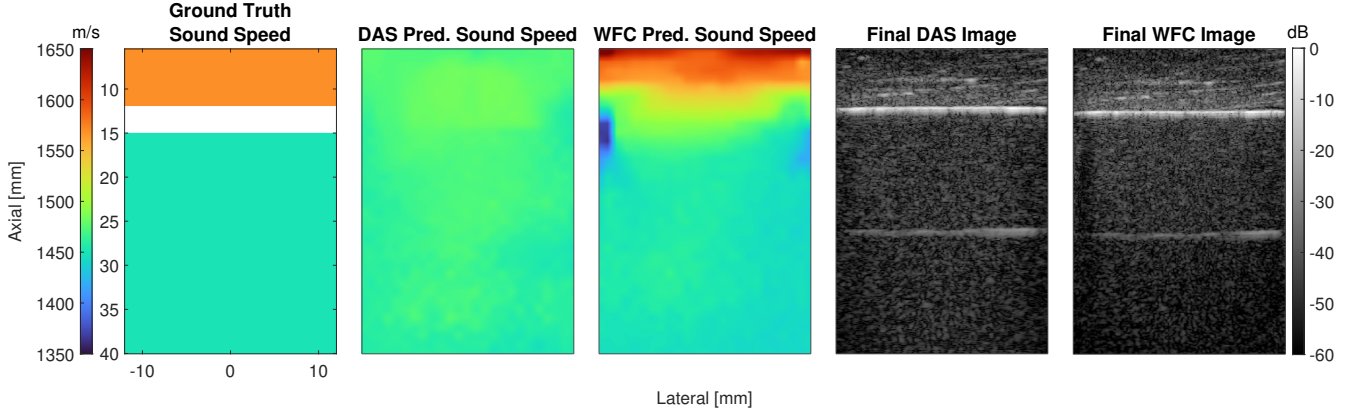


Fig. 3: Sound speed estimations for an acquisition with chicken over a constant sound speed phantom. The ground truth sound speeds based on calibration measurements or phantom specifications are shown on the left. A small region is excluded about the boundary between the chicken and phantom (shown in white). The chicken region appears clearly in the WFC sound speed estimation, with much lower bias compared to the DAS estimate, and the phantom region has lower error using WFC compared to DAS.

the DAS-estimate beamformed image, and -47.0 dB for the WFC-estimate beamformed image. The point target resolution and intensity improvements indicate that the WFC-estimated sound speed map has relatively higher accuracy compared to the DAS-estimated sound speed map.

C. In Vivo

Representative sound speed estimates and beamformed image comparisons for thyroid acquisitions from two subjects at different acquisition locations are shown in Figure 5. Although the ground truth sound speeds are unknown, the images using local sound speed maps show resolution and contrast improvements from aberration correction compared to beamforming with a constant sound speed that was used to initialize the optimization process. Contrast improvements are detailed in Table IV, with regions of interest indicated by arrows on the corresponding figures. The gCNR comparisons show that WFC results in the best contrast in hypoechoic and anechoic regions. Additionally, using the estimated sound speed maps results in improved resolution in the final aberration-corrected images. In Figure 5a, the scatterer in the center of the third inclusion has a lateral -6 dB width of 1.39 mm when beamforming with a constant sound speed. Using the DAS sound speed during beamforming results in a 0.72 mm -6 dB width, and using the WFC sound speed results in a 0.69 mm width. Similarly in Figure 5b, the scatterers surrounding the structure in the green box have the best resolution for the image beamformed using the WFC sound speed estimation, with improvements in lateral resolution as much as 0.14 mm compared to using a constant sound speed and 0.03 mm compared to using the DAS sound speed prediction.

Estimations for a rat liver acquisition with more tissue heterogeneity are shown in Figure 6. The measured global sound speed of the liver was 1562 m/s, resulting in an overall bias of -40 m/s for the DAS sound speed estimate and 11 m/s for the WFC sound speed estimate. The WFC estimate appears to distinguish different tissue regions more clearly than the

DAS estimate. The abdominal wall above 5 mm appears more clearly as a different sound speed region from the rest of the liver. Additionally, the tissue region on the upper left appears as an entire region with lower sound speed in the WFC estimate, while only part of that region in the upper center of the liver has a lower sound speed in the DAS estimate. The aberration-corrected WFC image demonstrates improved image quality, especially on the left side, compared to the DAS image. The largest hypoechoic region around -10 mm laterally and 15 mm axially has a gCNR of 0.93 for the WFC image and a gCNR of 0.87 for the DAS image. The -6 dB lateral width for the stronger scatterers between -5 and -10 mm laterally and 10 and 15 mm axially decreases up to 0.18 mm in the WFC image compared to the DAS image. Even on the upper right, the strong scatterer at 6 mm laterally and 4 mm axially shows a slight lateral -6 dB resolution improvement of 0.06 mm for WFC relative to DAS.

V. DISCUSSION

A. Sound Speed Estimation and Aberration Correction Enhancements

A major difference in the sound speed estimates from the WFC model is the accuracy in the sound speed values and structure compared to DAS with a straight-ray travel path assumption. By simulating the wave propagation through a heterogeneous medium, the refraction and diffraction of the waves is included in the wave propagation model, which is more accurate than a straight-ray assumption that does not include refraction or diffraction. This effectively results in more

TABLE IV: *In Vivo* Thyroid gCNR Comparisons

Region	Initial gCNR	DAS gCNR	WFC gCNR
Fig. 5a Inclusion 1	0.68	0.66	0.84
Fig. 5a Inclusion 2	0.67	0.82	0.86
Fig. 5a Inclusion 3	0.84	0.92	0.93
Fig. 5b Inclusion 1	0.81	0.87	0.86
Fig. 5b Inclusion 2	0.66	0.76	0.85

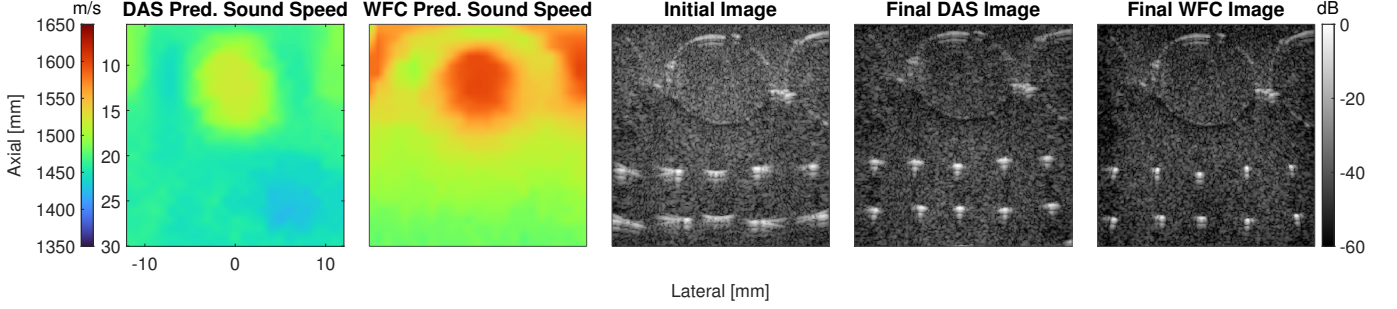


Fig. 4: Sound speed estimation and aberration correction comparisons for a fabricated alcohol-gelatin phantom. The difference between the inclusion and background sound speeds is around 25 m/s higher in the WFC prediction compared to the DAS prediction, and the background sound speed is more uniform for WFC compared to DAS. While the point target resolution improves with aberration correction from using a local sound speed map compared to using a constant sound speed, the final image using the WFC-estimated sound speed map leads to better lateral point target resolution compared to using the DAS-estimated sound speed.

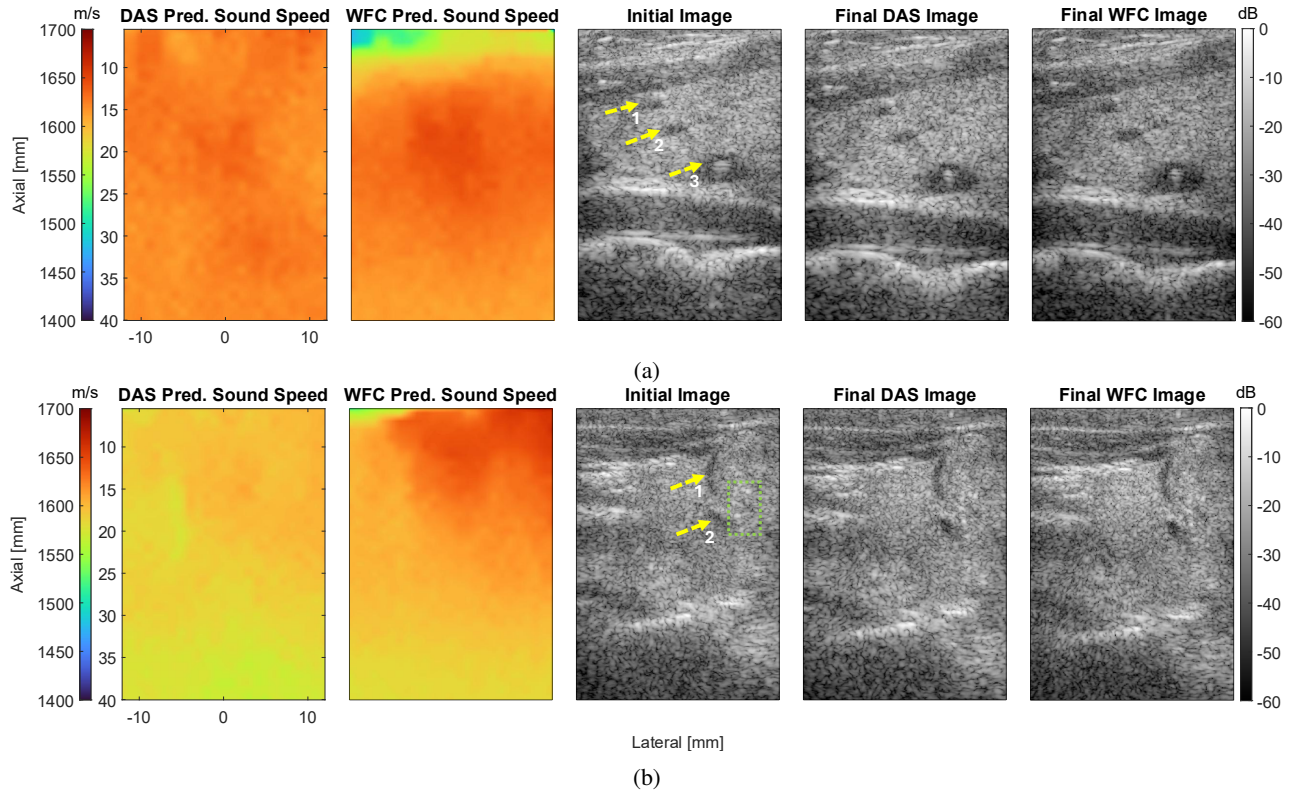


Fig. 5: Sound speed estimates and aberration corrected images for thyroid acquisitions from different subjects. Regions of interest for gCNR calculations are indicated by arrows. The contrast in hypoechoic and anechoic regions improves more greatly for the WFC model compared to the straight-ray DAS model. Some stronger scatterers exhibit improvements to resolution, especially when compared to using a constant sound speed to beamform, such as the scatterer in inclusion 3 in (a) or the scatterers forming the boundary of the structure in the green box in (b).

accurate beamforming in heterogeneous media, especially with larger sound speed variations, and more accurate estimation of the sound speed structure, as exemplified by the shape of the inclusions in Figure 4. The ground truth sound speeds were not measured for this inclusion phantom, but the material composition formulas used in Ali et al. [24] suggest the target sound speeds were 1650 and 1515 m/s for the inclusions and background, respectively. Although these sound speeds cannot

be guaranteed, a higher sound speed estimate can be observed in both the inclusion and background of this phantom when using WFC compared to straight-ray DAS. While sound speed estimates from the straight-ray model can result in a visible improvement to the final aberration-corrected image, a more accurate sound speed map can further improve the image, as well as provide more reliable sound speed estimates for use in quantitative biomarkers of disease. Additionally, due

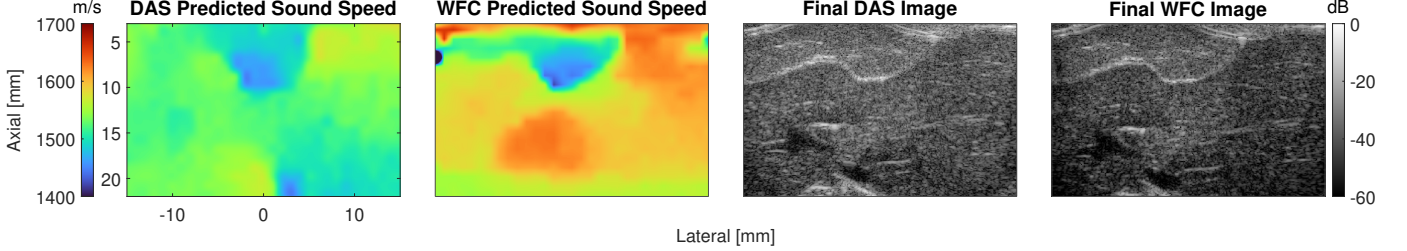


Fig. 6: Sound speed estimation and aberration correction comparisons for an *in vivo* rat liver acquisition. The abdominal wall appears more clearly as a different sound speed from the liver region in the WFC sound speed estimate compared to the DAS estimate, and most of the tissue structure visible in the upper left of the beamformed images appears as a distinct region with lower sound speed in the WFC estimate, compared to the DAS estimate that only shows a section centered at approximately 0 mm laterally as a lower sound speed. The WFC aberration corrected image shows improved resolution and contrast, especially on the left half.

to the spatiotemporal matched filtering from the correlation of an idealized forward-propagated transmit wavefield and the backward-propagated actual received wavefield, the effect of diffuse clutter can be reduced using WFC, which can improve the calculation of image quality metrics which would otherwise be adversely affected by reverberation noise. This results in more accurate sound speed estimations in cluttered scenarios, such as the reverberation shown in the lumen of the vasculature in Fig. 5. However, this spatiotemporal matched filtering only occurs with the one-way propagation simulation method used here. A two-way propagation model, such as k-Wave or Fullwave, will match the reverberation signal from propagation of the reflected waves and will thus not cancel multiple reflections.

Some small artifacts worth noting in some of the WFC sound speed estimation results are the corner artifacts in the two simulation cases in Figure 2 and the sound speed dips on the edges of the meat-layer phantom in Figure 3. These features do not consistently appear for all sources of data, but they could potentially be mitigated through different regularization parameters or setup, changes to the field of view covered by the points in the loss calculation grid, or different initialization parameters.

B. Optimization Approach

An advantage of auto-differentiation to optimize sound speed through gradient descent is the relative ease through which arbitrary loss criteria without an explicitly calculated gradient can be backpropagated to update a variable of interest, as long as all operations taken to calculate the loss with respect to that variable are backwards differentiable in software. Wavefield correlation as described in this work is a fully differentiable approach that accounts more accurately for wave propagation in a heterogeneous medium. Calculating Eikonal time delays is an alternative approach that accounts for refraction compared to the simpler straight ray approximation, but typical Eikonal equation solvers are not differentiable [35]. Additionally, the CMPE metric, which can be calculated in a differentiable way using separate sub-aperture split-step angular spectrum simulations, results in better sound speed estimates compared to other image focus metrics, as shown

in [19] and [36]. However, this optimization approach can have several disadvantages, some of which are similar to other sound speed estimators for pulse-echo ultrasound. Tracking all operations and necessary variable values to perform software auto-differentiation requires a considerable amount of memory, and can easily require high-end GPUs with more vRAM when utilizing GPU code acceleration. While DAS beamformers can benefit more from the GPU acceleration and have fewer operations to track, the angular spectrum simulation used for WFC must run sequentially in depth, resulting in longer runtimes, and more computational steps result in higher memory needs. However, this style of optimization at this stage of development must be performed offline anyway due to the gradient-descent-style iterative loss minimization. To reduce the runtime by requiring fewer iterative steps, a heterogeneous local sound speed map, obtained from a real-time sound speed estimator, could be used to initialize the optimization closer to the actual sound speed. Additionally, loss metrics that are faster to calculate than CMPE could be used for some or all parts of the iteration process.

Similar to other sound speed estimators, a few components in the algorithm require manual tuning or adjustment. Regularization has a large impact on the morphology of the final result due to the ill-posedness of the pulse-echo local estimation problem. Simply optimizing for an image metric by itself often does not result in a physically possible sound speed map, especially in cluttered data, due to the large, rapid variations or extreme values that will develop in the sound speed map. Regularization, therefore, must be added to the optimized loss, with the exact weight tuned for different media to enforce a balance in realistic smoothness and sound speed variation. Additionally, the stopping criterion is not standardized in this work and was set to a number of iterations for which the sound speed estimation settled to stable values. To more adaptively stop the iteration process, a stopping criterion can be defined based on the CMPE, which could further reduce the runtime.

C. Initialization and Pulse-Echo Depth-Velocity Ambiguity

Due to the extreme non-convexity and ill-posedness of the optimization problem, the initialization greatly affects the global (mean) sound speed and, consequently, the bias in the

final sound speed map. The effect of the initialization on the final global sound speed offset has been demonstrated for other pulse-echo local sound speed estimators, like Figure 5 in [24]. While the exact global sound speed, and thus the spatial locations of structures in the beamformed image, heavily depends on the constant sound speed used for initialization, aberration is still corrected to a similar degree in the final image using the estimated sound speed. Different initializations, coupled with differences in the field of view used, can also affect the final sound speed estimation results, as seen when comparing the fabricated inclusion phantoms in Figure 4 and the same phantom estimates in [19] with a different field of view and initialization parameters. This phenomenon is caused by depth-velocity ambiguity in pulse-echo measurements, where the exact location of objects in a medium cannot be determined if the sound speed is unknown. This ambiguity is presented in theoretical detail in [37], and similar occurrences of depth-velocity ambiguity in iterative sound speed estimation heavily influenced by initialization are discussed in [24] and [38]. Although depth-velocity ambiguity can make the exact sound speed values estimated less reliable to directly use for downstream applications, the relative change in sound speed in the map is still useful for applications like aberration correction. Regardless of the location of features due to the global sound speed offset, resolution and contrast still improve from accounting for the relative time delay changes caused by changing sound speed in media.

An approach to reduce the effects of initialization is calibration (which can additionally account for modeling errors). Tomographic inversion approaches to estimating sound speed use phase shift calibration for different starting sound speeds to account for modeling errors [39]. For an iterative sound speed estimation approach, [19] instead utilizes an additional scalar time offset that is calibrated for individual sources of data. This time offset essentially accounts for portions of the wave propagation process that are not modeled, such as the transducer lens and 3D propagation. This time offset is chosen to minimize the sound speed bias for known homogeneous sound speed data for each data collection scenario, requiring separate calibration for both simulation and different scanned media to reduce estimation bias. While calibration is more reliable in reducing the global bias, it either requires pre-calibration for each imaging scenario and starting sound speed, or knowing the sound speed in a medium, which could complicate standard clinical *in vivo* imaging applications. In this work, both the initial sound speed and a time offset are both swept prior to the initial beamforming iteration to find the pair of values that optimizes the CMPE. While this can result in lower estimation bias than simply sweeping for a starting sound speed, the initialization can have greater variation based on factors such as the exact medium imaged, field of view, or number of elements used during beamforming.

However, to better address the global sound speed bias without calibration, future approaches would either need to overcome the depth-velocity ambiguity, or reliably initialize the sound speed and accurately model the exact wave propagation for scanner data. Better modeling of wave propagation through the transducer lens, as in [40], could reduce the

need for applying a time offset to account for propagation inaccuracies. Additionally, initialization could be posed as a separate problem to optimize by itself due to the strong influence of the initial sound speed on the final global sound speed of the estimate. For example, a hyperparameter tuning approach could be utilized to find the optimal parameters for initialization, as well as the rest of the optimization process.

VI. CONCLUSION

We present an approach to local sound speed estimation that improves estimates in challenging heterogeneous media, especially cases with reverberation clutter and large changes in sound speed. The proposed estimator optimizes sound speed by implementing the WFC beamformer, which involves simulating transmit and receive wavefield propagation, using auto-differentiation software. A total-variation regularized CMPE loss is calculated from beamformed data, and a local sound speed map is iteratively updated using gradient descent, with the backpropagated gradient automatically computed through software. We compare sound speed estimates and aberration correction for this beamformer with a previously-published straight-ray DAS approach, showing larger estimated sound speed variation between different media regions, decreased estimation error, and improved image resolution and contrast. These results show promise for extending pulse-echo sound speed estimation to more challenging *in vivo* imaging situations with significant clutter and sound speed changes.

ACKNOWLEDGMENT

The authors would like to thank the Dahl Lab beamforming group for their helpful discussions and insight.

REFERENCES

- [1] R. Ali, T. Brevett, L. Zhuang, H. Bendjador, A. S. Podkowa, S. Hsieh, W. Simson, S. J. Sanabria, C. Herickhoff, and J. J. Dahl, "Aberration correction in diagnostic ultrasound: A review of the prior field and current directions," *Z. Med. Phys.*, vol. 33, no. 3, pp. 267–291, 2023.
- [2] Y. Deng, M. L. Palmeri, N. C. Rouze, G. E. Trahey, C. M. Haystead, and K. R. Nightingale, "Quantifying image quality improvement using elevated acoustic output in B-mode harmonic imaging," *Ultrasound Med. Biol.*, vol. 43, no. 10, pp. 2416–2425, 2017.
- [3] A. Smereczyński and K. Kołaczyk, "Pitfalls in ultrasound imaging of the stomach and the intestines," *J. Ultrason.*, vol. 18, no. 74, pp. 207–211, 2018.
- [4] M. Jaeger, E. Robinson, H. G. Akarçay, and M. Frenz, "Full correction for spatially distributed speed-of-sound in echo ultrasound based on measuring aberration delays via transmit beam steering," *Phys. Med. Biol.*, vol. 60, no. 11, pp. 4497–4515, 2015.
- [5] M. Jaeger, G. Held, S. Peeters, S. Preisser, M. Grüning, and M. Frenz, "Computed ultrasound tomography in echo mode for imaging speed of sound using pulse-echo sonography: Proof of principle," *Ultrasound Med. Biol.*, vol. 41, no. 1, pp. 235–250, 2015.
- [6] S. J. Sanabria, E. Ozkan, M. Rominger, and O. Goksel, "Spatial domain reconstruction for imaging speed-of-sound with pulse-echo ultrasound: simulation and *in vivo* study," *Phys. Med. Biol.*, vol. 63, no. 21, p. 215015, Oct. 2018.
- [7] P. Stähli, M. Kuriakose, M. Frenz, and M. Jaeger, "Improved forward model for quantitative pulse-echo speed-of-sound imaging," *Ultrasonics*, vol. 108, p. 106168, 2020.
- [8] R. Rau, D. Schweizer, V. Vishnevskiy, and O. Goksel, "Speed-of-sound imaging using diverging waves," *Int. J. Comput. Assist. Radiol. Surg.*, vol. 16, no. 7, pp. 1201–1211, 2021.

[9] M. Jakovljevic, S. Hsieh, R. Ali, G. Chau Loo Kung, D. Hyun, and J. J. Dahl, "Local speed of sound estimation in tissue using pulse-echo ultrasound: Model-based approach," *J. Acoust. Soc. Am.*, vol. 144, no. 1, pp. 254–266, July 2018.

[10] R. Ali, A. V. Telichko, H. Wang, U. K. Sukumar, J. G. Vilches-Moure, R. Paulmurugan, and J. J. Dahl, "Local sound speed estimation for pulse-echo ultrasound in layered media," *IEEE Trans. Ultrason., Ferroelectr., Freq. Control*, vol. 69, no. 2, pp. 500–511, 2022.

[11] R. Ali and J. J. Dahl, "Distributed phase aberration correction techniques based on local sound speed estimates," in *Proc. 2018 IEEE Int. Ultrason. Symp. (IUS)*, 2018, pp. 1–4.

[12] S. Beuret, D. Perdios, and J.-P. Thiran, "Refraction-aware integral operator for speed-of-sound pulse-echo imaging," in *Proc. 2020 IEEE Int. Ultrason. Symp. (IUS)*, 2020, pp. 1–4.

[13] R. Ali, T. Brevett, D. Hyun, L. L. Brickson, and J. J. Dahl, "Distributed aberration correction techniques based on tomographic sound speed estimates," *IEEE Trans. Ultrason., Ferroelectr., Freq. Control*, vol. 69, no. 5, pp. 1714–1726, 2022.

[14] R. Ali, T. Mitcham, M. Singh, R. Bouchard, M. Doyley, J. Dahl, and N. Duric, "Iterative sound speed tomography for distributed aberration correction," in *Proc. 2023 IEEE Int. Ultrason. Symp. (IUS)*, 2023, pp. 1–4.

[15] Y. Zengqiu, W. Wu, L. Xiao, E. Zhou, Z. Cao, J. Hua, and Y. Wang, "Iterative pulse-echo tomography for ultrasonic image correction," *Sensors*, vol. 24, no. 6, 2024.

[16] S. Krishnan, P.-C. Li, and M. O'Donnell, "Adaptive compensation of phase and magnitude aberrations," *IEEE Trans. Ultrason., Ferroelectr., Freq. Control*, vol. 43, no. 1, pp. 44–55, 1996.

[17] S.-E. Måsøy, T. Varslot, and B. Angelsen, "Iteration of transmit-beam aberration correction in medical ultrasound imaging," *J. Acoust. Soc. Am.*, vol. 117, no. 1, pp. 450–461, 01 2005.

[18] J. Wang, T. Zhou, G. Zhang, B. Li, X. Liu, and D. Ta, "Pixel-responsive optimization beamforming method for ultrasound transcranial imaging," *Med. Imag. Anal.*, vol. 106, p. 103762, 2025.

[19] W. Simson, L. Zhuang, B. N. Frey, S. J. Sanabria, J. J. Dahl, and D. Hyun, "Ultrasound autofocusing: Common midpoint phase error optimization via differentiable beamforming," *IEEE Trans. Med. Imag.*, pp. 1–1, 2025.

[20] J. Schleicher, J. C. Costa, and A. Novais, "A comparison of imaging conditions for wave-equation shot-profile migration," *Geophysics*, vol. 73, no. 6, pp. s219–s227, 2008.

[21] H.-M. Schwab and G. Schmitz, "Full-wave ultrasound reconstruction with linear arrays based on a fourier split-step approach," in *Proc. 2018 IEEE Int. Ultrason. Symp. (IUS)*, 2018, pp. 1–4.

[22] R. Ali, "Fourier-based synthetic-aperture imaging for arbitrary transmissions by cross-correlation of transmitted and received wave-fields," *Ultrason. Imaging*, vol. 43, no. 5, pp. 282–294, 2021.

[23] L. Zhuang, T. Brevett, D. Hyun, and J. Dahl, "Simultaneous reverberation noise reduction and aberration correction using wavefield correlation," in *Proc. 2024 IEEE Int. Ultrason. Symp. (IUS)*, 2024, pp. 1–5.

[24] R. Ali, T. M. Mitcham, M. Singh, M. M. Doyley, R. R. Bouchard, J. J. Dahl, and N. Duric, "Sound speed estimation for distributed aberration correction in laterally varying media," *IEEE Trans. Comput. Imag.*, vol. 9, pp. 367–382, 2023.

[25] J. Rao, A. Saini, J. Yang, M. Ratassepp, and Z. Fan, "Ultrasonic imaging of irregularly shaped notches based on elastic reverse time migration," *NDT E Int.*, vol. 107, p. 102135, 2019.

[26] R. M. Jones and K. Hyynnen, "Comparison of analytical and numerical approaches for CT-based aberration correction in transcranial passive acoustic imaging," *Phys. Med. Biol.*, vol. 61, no. 1, p. 23, Nov. 2015.

[27] J. F. Claerbout, "Toward a unified theory of reflector mapping," *Geophysics*, vol. 36, no. 3, pp. 467–481, 06 1971.

[28] R. Mallart and M. Fink, "Adaptive focusing in scattering media through sound-speed inhomogeneities: The van Cittert Zernike approach and focusing criterion," *J. Acoust. Soc. Am.*, vol. 96, no. 6, pp. 3721–3732, 12 1994.

[29] G. F. Pinton, J. Dahl, S. Rosenzweig, and G. E. Trahey, "A heterogeneous nonlinear attenuating full-wave model of ultrasound," *IEEE Trans. Ultrason., Ferroelectr., Freq. Control*, vol. 56, no. 3, pp. 474–488, 2009.

[30] G. Pinton, "A fullwave model of the nonlinear wave equation with multiple relaxations and relaxing perfectly matched layers for high-order numerical finite-difference solutions," *arXiv preprint arXiv:2106.11476*, 2021.

[31] L. Zhuang, O. Ostrasz, M. Sode, W. Simson, D. Hyun, F. Santibanez, J. Dahl, and G. Pinton, "Labeled numerical phantom of abdominal wall for wave-physics based ultrasound imaging: applications to image reconstruction," *IEEE Trans. Ultrason.*, pp. 1–1, 2025.

[32] A. V. Telichko, R. Ali, T. Brevett, H. Wang, J. G. Vilches-Moure, S. U. Kumar, R. Paulmurugan, and J. J. Dahl, "Noninvasive estimation of local speed of sound by pulse-echo ultrasound in a rat model of nonalcoholic fatty liver," *Phys. Med. Biol.*, vol. 67, no. 1, p. 015007, jan 2022.

[33] L. L. Brickson, D. Hyun, M. Jakovljevic, and J. J. Dahl, "Reverberation noise suppression in ultrasound channel signals using a 3D fully convolutional neural network," *IEEE Trans. Med. Imag.*, vol. 40, no. 4, pp. 1184–1195, 2021.

[34] A. Rodriguez-Molares, O. M. H. Rindal, J. D'hooge, S.-E. Måsøy, A. Austeng, M. A. Lediju Bell, and H. Torp, "The generalized contrast-to-noise ratio: A formal definition for lesion detectability," *IEEE Trans. Ultrason., Ferroelectr., Freq. Control*, vol. 67, no. 4, pp. 745–759, 2020.

[35] J. A. Sethian and A. M. Popovici, "3-D traveltime computation using the fast marching method," *Geophysics*, vol. 64, no. 2, pp. 516–523, 1999.

[36] B. N. Frey, D. Hyun, W. Simson, L. Zhuang, H. S. Hashemi, M. Schneider, and J. J. Dahl, "UltraFlex: Iterative model-based ultrasonic flexible-array shape calibration," *IEEE Trans. Ultrason., Ferroelectr., Freq. Control*, vol. 72, no. 11, pp. 1462–1475, 2025.

[37] A. S. Podkowa and M. L. Oelze, "The convolutional interpretation of registration-based plane wave steered pulse-echo local sound speed estimators," *Phys. Med. Biol.*, vol. 65, no. 2, p. 025003, Jan. 2020.

[38] R. Ali, T. Mitcham, M. Singh, R. Bouchard, J. Dahl, M. Doyley, and N. Duric, "Distributed aberration correction in handheld ultrasound based on tomographic estimates of the speed of sound," in *Med. Imag. 2023: Ultrason. Imag. Tomogr.*, C. Boehm and N. Bottenus, Eds., vol. 12470, International Society for Optics and Photonics. SPIE, 2023, p. 1247009.

[39] M. Jaeger, P. Stähli, N. Korta Martiartu, P. Salemi Yolgunlu, T. Frappart, C. Fraschini, and M. Frenz, "Pulse-echo speed-of-sound imaging using convex probes," *Phys. Med. Biol.*, vol. 67, no. 21, p. 215016, Oct. 2022.

[40] R. Waasdorp, D. Maresca, and G. Renaud, "Assessing transducer parameters for accurate medium sound speed estimation and image reconstruction," *IEEE Trans. Ultrason., Ferroelectr., Freq. Control*, vol. 71, no. 10, pp. 1233–1243, 2024.